



Real-space renormalisation approach to the Chalker–Coddington model revisited: Improved statistics

Syl Shaw^{*}, Rudolf A. Römer

Department of Physics, University of Warwick, Gibbet Hill Road, Coventry, CV4 7AL, United Kingdom

ARTICLE INFO

Editor: Horacio Pastawski

Dataset link: <https://wrap.warwick.ac.uk/184136/>

Keywords:

Quantum Hall effect
Phase transition
Localisation
Critical exponent
Renormalisation
Chalker–Coddington model
Real-space renormalisation group
Geometric disorder

ABSTRACT

The real-space renormalisation group method can be applied to the Chalker–Coddington model of the quantum Hall transition to provide a convenient numerical estimation of the localisation critical exponent, ν . Previous such studies found $\nu \sim 2.39$ which falls considerably short of the current best estimates by transfer matrix ($\nu = 2.593^{+0.005}_{-0.006}$) and exact-diagonalisation studies ($\nu = 2.58(3)$). By increasing the amount of data 500 fold we can now measure closer to the critical point and find an improved estimate $\nu = 2.51^{+0.11}_{-0.11}$. This deviates only $\sim 3\%$ from the previous two values and is already better than the $\sim 7\%$ accuracy of the classical small-cell renormalisation approach from which our method is adapted. We also study a previously proposed mixing of the Chalker–Coddington model with a classical scattering model which is meant to provide a route to understanding why experimental estimates give a lower $\nu \sim 2.3$. Upon implementing this mixing into our RG unit, we find only further increases to the value of ν .

1. Introduction

The plateau transitions of the quantum Hall effect (QHE) have retained interest over numerous decades [1–14]. At least four reasons come to mind that might explain this continuing attention: (i) the QHE offers a fairly accessible approach, both theoretically and experimentally, to studying the interplay of many-body interactions and disorder, due to its low-dimensionality, its ready realisation in well-understood semiconductor platforms and its by now fairly accommodating magnetic-field requirements [15–18]. Next, (ii) the QHE exhibits the simplest of the topological phase transitions, serving both as a springboard into the field and a convenient benchmark case for the many advances in topological systems in the last decade [19–25]. Still, the QHE also retains some of its mysteries with (iii) ongoing interest in its microscopic mechanisms [26–28] and the importance of interactions in both integer and fractional QHEs [29–34] and (iv) the remaining discrepancies between experimental measurements and theoretical predictions [35–37].

The precise value of the critical exponent governing the plateau-to-plateau transitions, even in the integer QHE, is a particularly intriguing such mystery [38]. While experimental results seem to have converged towards a value of $\nu = 2.38$ [37], high-precision numerical studies have decisively shifted from earlier estimates, then in reasonable agreement with the experimental values, to a significantly higher value of $\nu =$

2.59 ± 0.01 [36,39]. This later increase comes from three independent improvements, namely (1) studies with increased system sizes, allowing the analysis to move ever closer to the transition point, (2) better theoretical modelling of the behaviour close to the transition with a more convincing treatment of irrelevant finite-size corrections and (3) an improvement in the statistics of the generated data. A similar such improvement of experimental data, which could be achieved by (1) lowering experimental temperature and (2) better control of experimental parameters, has not yet been undertaken, but might lead to a similarly increasing exponent. Nevertheless, in the absence of improved experimental results one is drawn to evaluating other theoretical approaches. In a series of papers [40,41], following on from [38], it was recently argued that a mix of classical and quantum networks can lead to a reduced estimate of ν to values again in agreement with experimental studies. Still, it remains unclear that such models can truly capture the QHE situation. Nevertheless, one should at least try and see if all the theoretical models formerly giving $\nu \sim 2.3$ can now be shown to consistently give ~ 2.6 when (1–3) are followed.

This program is what we present here for the case of the real-space renormalisation group (RSRG) to the Chalker–Coddington (CC) network model of the integer QHE, a method judiciously adapted from a similar RSRG for classical percolation [42]. In the CC model, the method had

^{*} Corresponding author.

E-mail addresses: syl.shaw@warwick.ac.uk (S. Shaw), r.roemer@warwick.ac.uk (R.A. Römer).

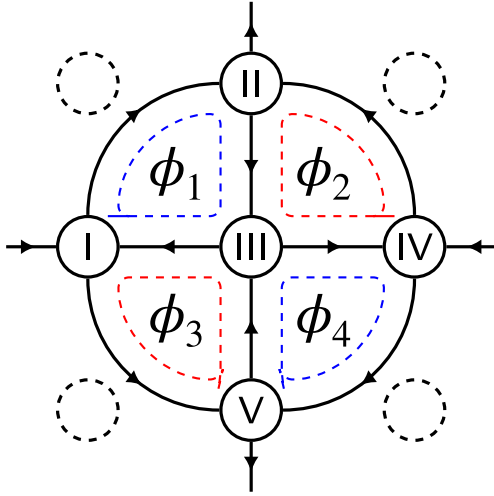


Fig. 1. The RSRG unit-cell of the CC model consisting of five saddle points. It is the smallest such construction which satisfies self-similarity with respect to edges. Nodes within the unit cell (circles) are labelled with roman numerals. Phases exist along each edge (arrowed lines) of the network, although in calculations these simplify to the four phases $\phi_1, \phi_2, \phi_3, \phi_4$, representing the phase accumulated upon traversing the edges associated with the dashed loop surrounding the label. The dashed circles represent ignored nodes.

previously been shown to give $\nu \sim 2.37$ [43]. This is better than what should have been expected since the RSRG in the classical percolation only produces the critical exponent of the percolation transition within $\sim 7\%$. As we will show here, by increasing the number of samples 500-fold, while also employing arbitrary-precision arithmetic [44], we now find a value of $\nu = 2.51 \pm 0.11$. In addition, we use the improved RSRG to also study the mixed problem of classical and quantum nodes proposed in [38,40] mentioned above. Sadly, we find that the problem is very sensitive to the geometry of the chosen renormalisation group (RG) unit. While fixed point distributions can be constructed and estimates of critical exponents can be found, these do not readily correspond to known universality classes.

2. Real-space renormalisation group on the Chalker–Coddington model

2.1. Scattering matrix approach to the QH transition

The CC model describes the magnetic-field-induced chiral transport in the integer QHE via a 2D lattice populated with nodes representing saddle points in a continuous potential landscape. Electron wave packets can travel along directed equipotential paths – clockwise or counterclockwise according to the direction of the magnetic field – and scatter between such paths via tunnelling across the saddlepoint nodes. Self-interference along the paths leads to localisation while the tunnelling enhances electron transport. Taken together, the effects combine such that in summary the CC model exhibits a localisation–delocalisation–localisation transition at a single energy, hence modelling the plateau-to-plateau transitions of the QHE. The CC model has been previously employed in many studies of integer QHE physics [35, 45–50]. In particular, when coupled with finite-size scaling, it can be used in transfer matrix studies to estimate the value of ν as discussed above [36].

Mathematically, each saddle point is represented by a 2×2 matrix S connecting two incoming, $\vec{I} = (I, I')$, with two outgoing channels, $\vec{O} = (O, O')$, as $\vec{O} = S \cdot \vec{I}$. Charge conservation is expressed via unitarity such that $|\vec{O}|^2 = \vec{O}^\dagger \vec{O} = \vec{I}^\dagger S^\dagger S \vec{I} = |\vec{I}|^2$ with \dagger representing a hermitian

conjugate. The most general complex-valued matrix S obeying these constraints is

$$S = \begin{bmatrix} \alpha & \beta \\ -\beta^* \exp i\phi & \alpha^* \exp i\phi \end{bmatrix} \quad (1)$$

with $\alpha, \beta \in \mathbb{C}$, $*$ the complex conjugate and ϕ a phase. Popular choices are

$$S = \begin{bmatrix} t & r \\ r & -t \end{bmatrix} \quad \text{and} \quad S = \begin{bmatrix} i \cos \theta & \sin \theta \\ \sin \theta & i \cos \theta \end{bmatrix}. \quad (2)$$

Here, $t, r \in \mathbb{R}$ refer to *transmission* and *reflection amplitudes* in the first representation with $|t|^2 + |r|^2 = 1$ [51] while the latter uses a single *mixing angle*, θ [3].

With reference to the potential landscape, an *effective saddle point height*, z , can be defined by [52]

$$\cos^2 \theta = t^2 = \frac{1}{1 + e^z}, \quad \sin^2 \theta = r^2 = \frac{1}{1 + e^{-z}}. \quad (3)$$

In the following, we shall denote the distribution of these parameters over all saddle points as $P(t)$, $P(z)$ and $P(\theta)$. A further parameter, of perhaps more direct experimental relevance, is the dimensionless *conductance* $G = t^2$ with $P(G) = P(t)/2t$. Furthermore, $P[t(z)] = P(z)|dt/dz| = e^z P[1/\sqrt{1 + e^z}]/2(1 + e^z)^{3/2}$ and $P[z(t)] = P(t)|dz/dt| = 2P[\ln(-1 + 1/t^2)]/(t - t^3)$.

2.2. RG determination of the fixed point distributions at the QH transition

Transfer matrix and diagonalisation studies of the CC model usually build up quasi-1D strips or 2D square lattices of saddle points and then proceed to compute localisation lengths, participation numbers, etc. [53,54]. The RSRG approach, on the other hand, works by considering a small subset of such a lattice structure via constructing an RG unit from several neighbouring nodes [52]. For the RG unit, we assemble the S matrices of each participating node into a *combined* S matrix and remove all unwanted connections to superfluous in- and outgoing channels such that we are only left with again two incoming and two outgoing channels. In Fig. 1, we show this RG unit graphically. We note that other RG units are possible, but none have thus far been shown to yield better results [43,55] than the 5-node RG unit depicted in Fig. 1. We emphasise that in drawing the figure, we have used the fact that the phases ϕ_j along the four closed loops j add. The five 2×2 S matrices combine into a single 10×10 matrix equation, previously shown in Refs. [43,55] in the t, r representation. Just as a single node has two incoming and outgoing channels, we have chosen the connections in the 5-node RG of Fig. 1 to have a similar effective *super-structure*. To determine the renormalised *super-parameters* of the entire 5-node RG one supplies an input to an incoming channel, say node I (or IV), and reads out at the outgoing channel V (or II, respectively). One can then find the effective renormalised t' analytically [52,56] by solving the aforementioned 10×10 matrix equation. Similarly, using the θ representation, we can analytically compute an RG equation for a renormalised mixing angle θ' , given as in Box I. Hence, starting with the five saddle points described by mixing angles θ_i , $i = 1, \dots, 5$ and the phases of the four closed loops $\phi_1, \phi_2, \phi_3, \phi_4$, we can compute the effective mixing angle θ' of the super-saddle point.

We are now ready to proceed with the RG process itself. We first need to construct a starting distribution P_1 of parameters. Then application of the RG equation for k RG generations will allow us to find the distribution of super-parameters P_k [52]. At criticality, we expect that $P_k \rightarrow P_{\text{FP}}$ for $k \rightarrow \infty$ with P_{FP} denoting the unstable fixed point (FP) distribution [43].¹

¹ Starting from a distribution too asymmetric or too far away from the P_{FP} , the RG flow will tend towards the stable classical FPs, e.g. $P(G) = \delta(G)$ or $P(G) = \delta(G - 1)$.

$$\cos \theta' = \frac{\begin{aligned} & -\cos \theta_1 [e^{i\phi_4} \cos \theta_3 \cos \theta_4 + i \cos \theta_5 (e^{i\phi_3} \sin \theta_2 \sin \theta_3 \sin \theta_4 - 1)] - e^{i\phi_1} \cos \theta_2 \cos \theta_3 \cos \theta_5 \\ & - i e^{i(\phi_1+\phi_4)} \cos \theta_4 \cos \theta_2 + i e^{i(\phi_1+\phi_4-\phi_2)} \cos \theta_2 \cos \theta_4 \sin \theta_1 \sin \theta_3 \sin \theta_5 \end{aligned}}{\begin{aligned} & e^{i\phi_4} \cos \theta_3 \cos \theta_4 \cos \theta_5 + e^{i\phi_1} \cos \theta_1 \cos \theta_2 \{ \cos \theta_3 + i e^{i\phi_4} \cos \theta_4 \cos \theta_5 \\ & + i [e^{i\phi_3} \sin \theta_2 \sin \theta_3 \sin \theta_4 + e^{i\phi_2} \sin \theta_1 (\sin \theta_3 - e^{i\phi_3} \sin \theta_2 \sin \theta_4) \sin \theta_5 - 1] \} \end{aligned}}. \quad (4)$$

Box I.

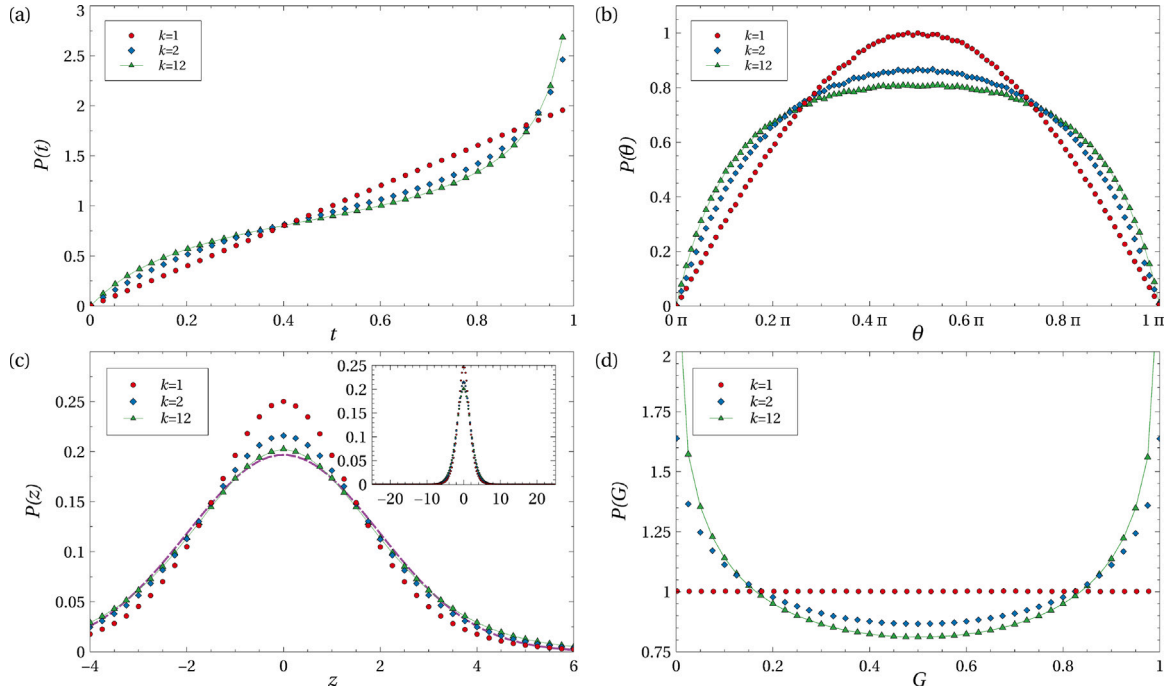


Fig. 2. Evolution of the distribution P of elements of the scattering matrix for RSRG steps $k = 1, 2$ and reaching close to convergence at $k = 12$ in the (a) $P(t)$, (b) $P(\theta)$, (c) $P(z)$ and (d) $P(G)$ representations. While in (a+b+d) the full range of t , θ and G is displayed, panel (c) shows a smaller z range for clarity while the full range $z \in [-25, 25]$ is given in the inset. The thin solid line in all panels is a guide to the eye for P_{12} . The dashed line in panel (c) shows a Gaussian fit to $P_{12}(z)$ for all $z \in [-25, 25]$.

While this procedure can in principle be done using any of the t , z , or θ representations, here we choose a combination of t and z representations for convenience [51]. We start with $P_1(t) = 2t$, equivalent to $P_1(z) = \frac{e^z}{(e^z+1)^2}$ (and $P_1(G) = 1$), and generate $P_2(t)$. The phases ϕ_i are chosen randomly in $[0, 2\pi]$ to model spatial variation among equipotentials. We then transform each t value to z and find $P_2(z)$. Cain et al. [51] have shown that the approach to the fixed point results in a sequence of symmetric distributions such that $P_k(z) = P_k(-z)$ with $\langle P_k(z) \rangle \approx 0$. Conversely, the symmetry can be enforced for each $P_k(z)$ and a symmetrised $P_k(z)$ with $\langle P_k(z) \rangle = 0$ constructed following the transformation relations given at the end of Section 2.1. This stabilises the approach to the fixed point distributions $P_{\text{FP}}(t)$, $P_{\text{FP}}(z)$, etc.

We implement this procedure and generate at least 5×10^9 z values for each RG generation k . This is about 500 times more than in previous such RG studies [57]. Since the generated super-distributions will be no longer comprised of simple functions, we employ the rejection method [58] to generate appropriate random numbers. Also, in the version implemented for this work, we use MATHEMATICA's arbitrary-precision arithmetic when evaluating Eq. (4) (in the t representation [51]). This reduces inevitable rounding errors when computing t and z values with usual compiler-based double precision arithmetic, allowing us to keep accurate track of z values ranging from $z_- = -25$ ($1 - t_+ \approx 10^{-11}$) to $z_+ = 25$ ($t_- \approx 10^{-11}$).

In Fig. 2, we show the resulting FP distributions for (a) $P(t)$, (b) $P(\theta)$, (c) $P(z)$ and (d) $P(G)$. We note that the spread of $P_{\text{FP}}(z)$ around $z = 0$ reflects the distribution of the disorder landscape. A fit to a

Gaussian for $z \in [-25, 25]$ can be obtained via a usual χ^2 minimisation taking into account the uncertainties of the $P_{\text{FP}}(z)$ values. However, a perfect fit is only achieved when we increase the uncertainties 8-fold. Nevertheless, the coefficient of determination is $R^2 > 0.99$ with $\langle P(z) \rangle = (0 \pm 2) \times 10^{-4}$ and standard deviation $\sigma = 2.17$. The fitted Gaussian curve is shown alongside the data in Fig. 2(c). We conclude that a Gaussian approximation is suitable, in particular for determining the maximum value of successive distributions with a restricted z range, and we use it below in determining the mean shift in saddle point heights.

2.3. Determination of an improved critical exponent

To determine the critical exponent ν , we next perturb the FP distribution by a constant shift z_0 , i.e. $P_{\text{FP}}(z) \rightarrow P_{\text{FP}}(z - z_0)$. We then observe how the perturbed distribution drifts away from criticality by monitoring the deviation of its maximum at z_{max} from 0 under repeated (unsymmetrised) RG steps [51]. Only the largest 4% of z values, corresponding approximately to all $z \in [z_0 - 1, z_0 + 1]$, are used to determine z_{max} by fitting to a Gaussian as shown in Fig. 3. After n such RG steps, we find that the position of the maximum follows $z_{\text{max}}(n) \propto z_0$ with good accuracy as detailed in Fig. 4. The critical exponent can then be computed via [52]

$$\nu = \frac{\ln 2^n}{\ln \left(\frac{z_{\text{max}}(n)}{z_0} \right)} \quad (5)$$

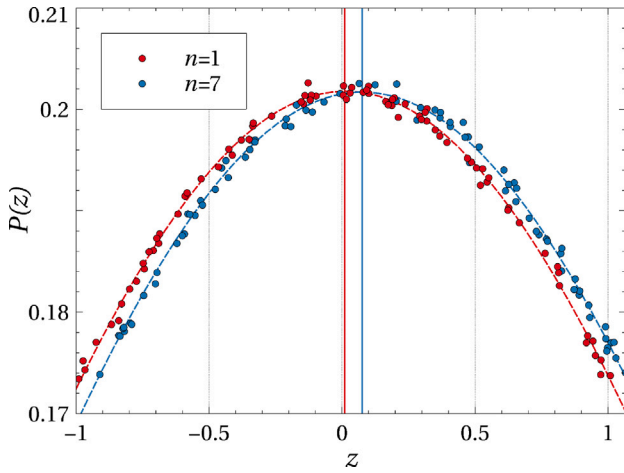


Fig. 3. Example of a shift of $P_{\text{FP}}(z)$ when perturbing with $z_0 = 0.1$. The data shown corresponds to $n = 1$ and $n = 7$, the lines indicate Gaussian fits and the two vertical lines show the obtained estimates for z_{max} . These two data values have been used when plotting Fig. 4. Vertical dashed grid lines mark $z = \pm 0.5$ and 1.

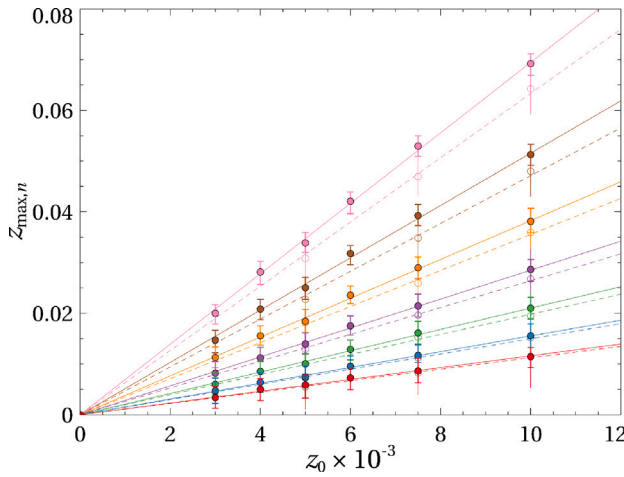


Fig. 4. Linear dependence of z_{max} on z_0 for six different starting values of z_0 s. Solid lines and markers indicate data without inclusion of the mixed model, whereas dashed lines with unfilled markers indicate data gathered from the mixed model with $p = 0.01$. Each set of lines corresponds to RG levels $n = 1, \dots, 7$ from bottom to top. The error bars for the CC model represent the highest and lowest values attained for five independent RSRG calculations with 10^9 z values each. The average value used henceforth is the mean of all 5 z_{max} values. For the mixed disorder model, the error is calculated from ten independent RSRG calculations for 10^8 z values. Each z_{max} datum is obtained via Gaussian fits as shown in Fig. 3. Lines represent the fits for z_n/z_0 according to Eq. (5).

and should converge for $n \rightarrow \infty$. As presented in Fig. 5, we find $\nu \approx 2.51^{+0.11}_{-0.11}$ for $n = 7$. In obtaining this increased ν value, the enhanced statistics of $P(z)$ allows us to study initial perturbations $z_0 = 0.003, 0.004, 0.005, 0.006, 0.0075$, and 0.01 . These values are ten times smaller than used previously, hence increasing the accuracy of the determination for ν . With $\nu = 2.593^{+0.005}_{-0.006}$ the accepted value from transfer matrix calculations [36], we find that our new result only deviates by 3.2%. This is of course very good when compared to the 7% accuracy in classical percolation [42].

3. Mixing classical and quantum percolation

While our new ν is now in better agreement with the high-precision estimates of Slevin and Ohtsuki [36] and Puschmann et al. [39], we have similarly increased the distance to the lower experimental estimates [11,37]. Work by Nuding et al. [59] and others [38,40] argue

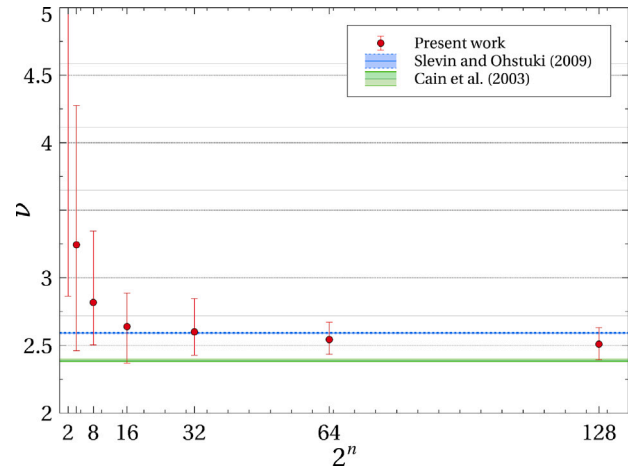


Fig. 5. A plot of ν as a function of system size 2^n , where n is the renormalisation step number. Seven RG steps are plotted. Each data point represents three values of z_0 averaged over 10 instances of our method, each instance consisting of 5×10^9 samples. We find the final value of ν to be $2.51^{+0.11}_{-0.11}$. The blue and green regions indicate reference values and associated errors found for ν previously [36,56], as indicated in the legend.

that this discrepancy could lie in the highly irregular arrangement of experimental scattering nodes which is nevertheless modelled on a square lattice in the CC model. They suggest that a mixed model, in which some nodes are left in the CC configuration, with t and r values, while other nodes are chosen fully open ($t = 1, r = 0$) or fully closed ($t = 0, r = 1$) with probability p , could lower the value of ν to be in better agreement with the experiments.

3.1. Fixed point distributions for the mixed model

This type of mixed disorder, termed “geometric disorder” by Gruzberg et al. [38], can be implemented into the RSRG method by intentionally modifying t values of the saddle points within the distributions. For distinction from the previous situation, we shall denote the resulting distributions as $Q_p(t), Q_p(z)$, etc. With this notation, $P(z) = Q_0(z)$. Upon every k th RG transformation each saddle point in the RG unit cell becomes, with probability p , either entirely transmitting ($t = 1$) or entirely reflecting ($t = 0$). Or, with probability $1 - 2p$, $p \leq 1/2$, the saddle point transmission amplitude remains a random number $\in [0, 1]$ selected from the previous distribution $Q_{p,k-1}(t)$, as before. But simply setting t values to 0 (i.e. $\theta = \pi$) in the analytic equation determining the renormalised t' (i.e. Eq. (4)) can result in a vanishing denominator. In terms of z , the $t = 0$ and 1 values correspond to $z = \pm\infty$, respectively. Hence we see a build-up of large $\pm z \approx 34$ values in $Q_{p,k+1}(z)$, which is increasing as k increases. Clearly, if we were to use such distributions in our RG procedure, we would effectively double-count the influx of the mixed disorder [55]. We avoid this by neglecting all accumulated z values beyond $z_{+,-} = \pm 25$ when computing $Q_{p,k+1}(z)$ in each RG step. Overall, the proportion of such events, $2 \int_{-\infty}^{\infty} Q_{p,k}(z) dz$, remains less than 10^{-5} as we try to approach a new $Q_{p,\text{FP}}(z)$.

In Fig. 6 we show that we can indeed find this new FP distribution for the case of mixed disorder for various p values. The fixed point distributions are again of roughly Gaussian shape with (e.g.) $\langle Q_{0.1}(z) \rangle = (0 \pm 2) \times 10^{-4}$ and $\Delta_p = |Q_{p,\text{FP}}(z) - Q_{\text{GauB}}(z)|/N = 1, 1, 2, 2, 3 (\times 10^{-3})$ for $p = 0.01, 0.025, 0.05, 0.075, 0.1$, respectively, where N denotes the number of bins used in constructing the $Q(z)$ distributions. In relation to P_{FP} , we note that the height-to-width ratio of $Q_{p=0.1,\text{FP}}(z)$ is about 0.62 times that of $Q_{p=0.0,\text{FP}}(z)$. The fixed point distributions with $p > 0$ have significantly longer z -tails, corresponding to a more rugged saddle point height landscape.

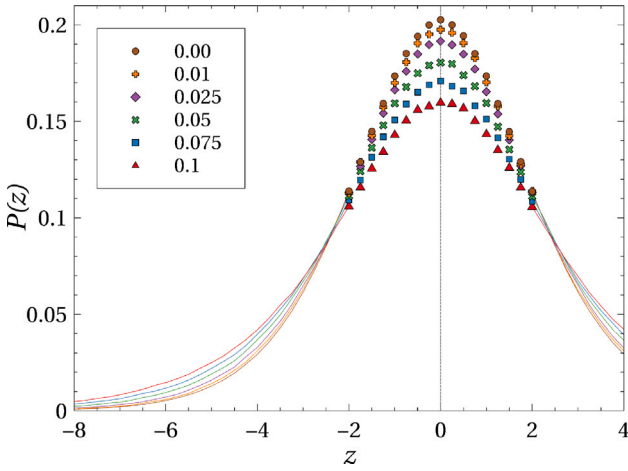


Fig. 6. Fixed point distributions $Q_0(z) (= P(z))$, $Q_{0.01}(z)$, ..., $Q_{0.1}(z)$ obtained with 1×10^9 RSRG evaluations. The values around $z = 0$ are indicated by symbols while we use lines otherwise. We also only show a small z -region $\in [-25, 25]$ for clarity. In calculations, we use the full z -range as displayed in the inset of Fig. 2(c).

The introduction of mixed disorder has no effect on the mean value of the $Q_{p,\text{FP}}(z)$ distribution, as random application of mixed disorder does not bias the effective saddle point heights in either direction. However, the introduction of p notably increases the amount of steps required to converge towards an FP distribution. This is shown in Fig. 7 with Δ_p plotted against RG iteration number k for varying values of p . Additionally, the shape of the FP distribution changes depending on p , as shown by the change in standard deviation σ_p converged upon for different p values also in Fig. 7. For larger p , we note a consistent increase in σ_p for each $Q_{p,\text{FP}}$.

3.2. Critical exponent for the mixed model

After having determined the FP distributions $Q_{p,\text{FP}}(z)$, we shift these as before by a small z_0 to determine the RG flow of the position on the maxima $z_{p,\text{max}}$. As indicated in Fig. 4, we find good linearity and can hence proceed to determine, for each p , a corresponding critical exponent of the mixed model, ν_p via Eq. (5). The results are astounding: the values of ν_p increase monotonically from $\nu_{p=0} = 2.51$ to $\nu_{p=1/3} = 4.9$ as shown in Table 1. Particularly the last number seems to indicate a behaviour at the QHE plateau-plateau transitions not found experimentally [60]. An increased value of ν up to $\nu_{p=0.4} = 3.276$ was indeed observed in Klümper et al. [40]. But the overall quantitative agreement of our results with these previous results across all p remains poor as shown in Fig. 8.

We find in particular that the agreement as a function of p is unsatisfactory. When considering the structure of the RG unit in Fig. 1, we note that the four corner nodes had been chosen to correspond to $t = 0$ and $t = 1$ in the opposing corners of the RG unit. So instead of simply ignoring these four corner nodes and concentrating on the five-node RG unit, it would be equally justified to include them into a now nine-node RG unit in which the four corner nodes are already part of the mixed model. This then suggests that one might introduce a normalised $p' = \frac{1}{2} \left(\frac{4}{9} + \frac{5(2p)}{9} \right) = \frac{2}{9} + \frac{5p}{9}$ with the $\frac{1}{2}$ in the initial expression chosen such that $2/9 \leq p' \leq 1/2$ also. In Fig. 8, we show the results for $\nu_{p'}$. Clearly, $\nu_{p'=2/9}$ is now in better agreement with the value of Klümper et al. [40]. But for other p' values, large differences remain.

Another source of systematic deviation from these results might be the small size of the RG unit and in particular, the privileged position of the central node, i.e. node three in Fig. 1. Effectively, it is the tunnelling across this node which allows for self-interference in a figure-of-eight arrangement [52]. In our implementation of the mixed model, we have

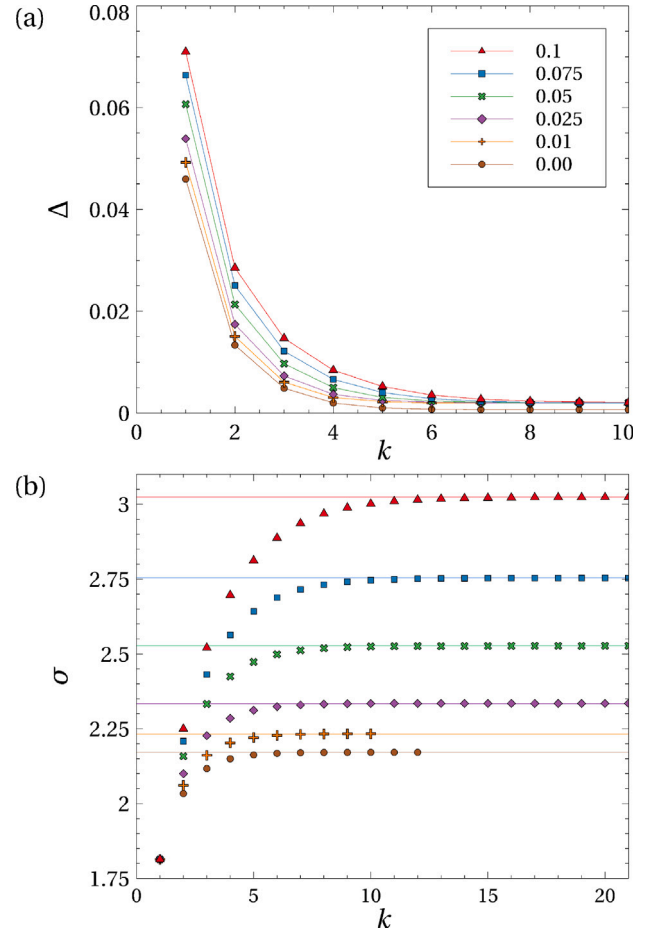


Fig. 7. A comparison of key parameters indicating convergence towards a fixed point distribution $Q_{p,\text{FP}}$ for multiple values of p . (a) shows the squared error between successive distributions $\Delta_p(k) = \int |Q_{k+1}(z) - Q_k(z)|^2 dz$ across 20 RG step iterations. (b) shows $\sigma_p(k)$ values as the number of RG steps increases. Plotting in (b) is consistent with the key in (a), but reversed to the key in Fig. 6 to follow the top-to-bottom order of the data. For all values of mixed disorder proportion p , the $Q_p(z)$ distribution converges. As p increases, more renormalisation steps are required for the distributions to converge. Lines in (a) are guides to the eye only while in (b) they indicate the converged values.

thus far allowed this node to also “percolate” with $t = 0$ and 1. Excluding this possibility requires to rescale p via $p^* = \frac{2}{9} + \frac{4p}{9}$ such that $2/9 \leq p^* \leq 4/9$. Our numerical results for ν both with and without this modification are displayed in Table 1. The modification results in even larger values for ν than previously, as shown in Fig. 8. Clearly, we seem stuck in a situation where the RG approach cannot reproduce the results of the mixed model.

4. Conclusion

The localisation length critical exponent, ν , of the quantum Hall transition can be estimated with the RSRG applied to the Chalker–Coddington model. Increasing the number of the statistical sample sizes 500 times, and using a more precise model for numerical data, has allowed us to get more stable and reliable estimates for $P(z)$. This in turn has enabled us to study the RSRG description of ν closer to the fixed point, being able to reduce z_0 by a factor of ten when compared to earlier RSRG approaches [56]. We find an increased estimate of $\nu \approx 2.51^{+0.11}_{-0.11}$. This is in line with the general trend observed in the past 2–3 decades when studying critical properties of second-order (quantum) phase transitions: substantially better statistics coupled with larger system sizes shift critical exponents towards $\sim 10\%$ larger values. This

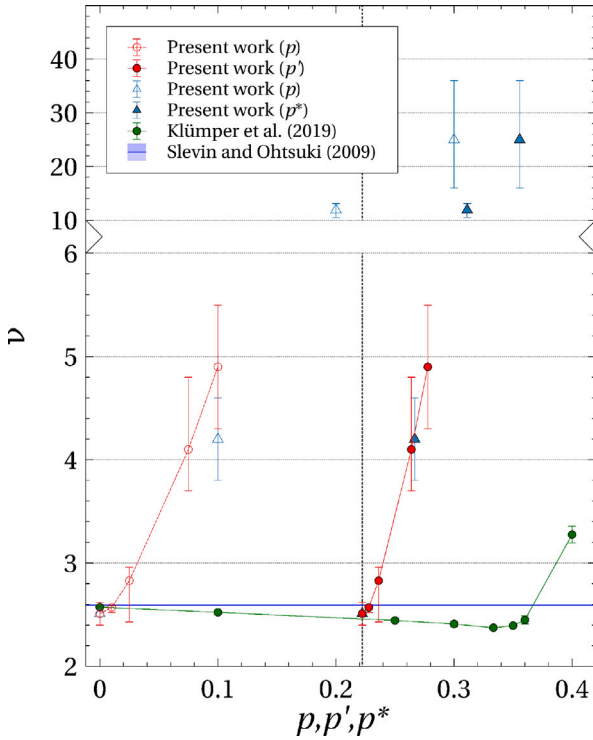


Fig. 8. Obtained estimates for ν compared with computed ν values from Ref. [40] for varying proportions of mixed disorder. Circles distinguish our results with all nodes affected by mixing, from triangles, which represent the data from the unit cell with the central node unaffected by the mixed disorder. Data transformed to p' and p^* are shown with filled-in markers (\bullet , \blacktriangle), whereas original p value markers have no fill (\circ , \triangle). Lines connecting ν estimates are guides to the eye only. The vertical dashed line indicates the horizontal probability value $2/9$.

Table 1

Values attained for the critical exponent ν when implementing the mixed disorder model at varying proportion levels p , p' and p^* in the RSRG. Data below the horizontal separator are generated excepting the central node from the mixing of models.

p	p'	p^*	ν
0	0.222		$2.51^{+0.11}_{-0.11}$
0.01	0.228		$2.58^{+0.03}_{-0.03}$
0.025	0.236		$2.83^{+0.13}_{-0.4}$
0.075	0.263		$4.1^{+0.7}_{-0.4}$
0.1	0.278		$4.9^{+0.6}_{-0.6}$
0.1		0.267	$4.2^{+0.4}_{-0.4}$
0.2		0.311	$11.9^{+1.2}_{-1.4}$
0.3		0.356	25^{+11}_{-9}

is true for the exponent of the QHE [36,39] as well as the 3D exponent of the Anderson metal–insulator transition [61–63]. A recent proposal for a deformed Wess–Zumino–Novikov–Witten type conformal field theoretic description of the QHE implies a resulting critical exponent $1/\nu \rightarrow 0$ [46], which would call for truly challenging computational resources or novel insight to allow a numerical validation.

For the mixed disorder model, proposed in Ref. [38], our results are inconclusive. Clearly, the model has its charms and attractions when discussed in connection to experimental results for the QHE. However, our current, very local RSRG cell fails to capture the expected behaviour of ν and returns rather unphysical results. Previous attempts to improve upon this by enlarging the RG cell have been shown to fail due to the inherent difficulties associated with such an approach [55].

CRediT authorship contribution statement

Syl Shaw: Writing – original draft, Visualization, Software, Investigation, Formal analysis, Data curation, Conceptualization. **Rudolf A. Römer:** Writing – review & editing, Supervision, Methodology, Conceptualization.

Declaration of competing interest

The authors declare that they have no known competing financial interests or personal relationships that could have appeared to influence the work reported in this paper.

Data availability

Data accompanying this publication are available at <https://wrap.warwick.ac.uk/184136/>.

Acknowledgements

We thank Warwick’s Scientific Computing Research Technology Platform for further computing time and support. UK research data statement: Data accompanying this publication are available at [64] while the code is at [65].

References

- [1] K. von Klitzing, T. Chakraborty, P. Kim, V. Madhavan, X. Dai, J. McIver, Y. Tokura, L. Savary, D. Smirnova, A.M. Rey, C. Felser, J. Gooth, X. Qi, 40 years of the quantum Hall effect, *Nat. Rev. Phys.* 2 (2020) 397–401.
- [2] S.M. Girvin, K. Yang, *Modern Condensed Matter Physics*, Cambridge University Press, 2019, <http://dx.doi.org/10.1017/9781316480649>.
- [3] J.H. Son, S. Raghu, Three-dimensional network model for strong topological insulator transitions, *Phys. Rev. B* 104 (2021) 125142.
- [4] M. Minkov, V. Savona, Haldane quantum Hall effect for light in a dynamically modulated array of resonators, *Optica* 3 (2016) 200.
- [5] K. Ohgushi, S. Murakami, N. Nagaosa, Spin anisotropy and quantum Hall effect in the Kagomé lattice: Chiral spin state based on a ferromagnet, *Phys. Rev. B* 62 (2000) R6065–R6068.
- [6] F.D.M. Haldane, Model for a quantum Hall effect without Landau levels: Condensed-matter realization of the “Parity Anomaly”, *Phys. Rev. Lett.* 61 (1988) 2015–2018.
- [7] S. Raghu, F.D.M. Haldane, Analogs of quantum-Hall-effect edge states in photonic crystals, *Phys. Rev. A* 78 (2008) 033834.
- [8] R.B. Laughlin, Quantized Hall conductivity in two dimensions, *Phys. Rev. B* 23 (1981) 5632–5633.
- [9] F. Tang, Y. Ren, P. Wang, R. Zhong, J. Schneeloch, S.A. Yang, K. Yang, P.A. Lee, G. Gu, Z. Qiao, L. Zhang, Three-dimensional quantum Hall effect and metal–insulator transition in ZrTe_5 , *Nature* 569 (2019) 537–541.
- [10] S.T. Hannahs, J.S. Brooks, W. Kang, L.Y. Chiang, P.M. Chaikin, Quantum Hall effect in a bulk crystal, *Phys. Rev. Lett.* 63 (1989) 1988–1991.
- [11] F. Hohls, U. Zeitler, R.J. Haug, R. Meisels, K. Dybko, F. Kuchar, Dynamical scaling of the quantum Hall plateau transition, *Phys. Rev. Lett.* 89 (2002) 276801.
- [12] K. Hashimoto, C. Sohrmann, J. Wiebe, T. Inoka, F. Meier, Y. Hirayama, R.A. Römer, R. Wiesendanger, M. Morgenstern, Quantum Hall transition in real space: From localized to extended states, *Phys. Rev. Lett.* 101 (2008) 256802.
- [13] N. d’Ambrumenil, B.I. Halperin, R.H. Morf, Model for dissipative conductance in fractional quantum Hall states, *Phys. Rev. Lett.* 106 (2011) 126804.
- [14] K. Hashimoto, T. Champel, S. Florens, C. Sohrmann, J. Wiebe, Y. Hirayama, R.A. Römer, R. Wiesendanger, M. Morgenstern, Robust nodal structure of Landau level wave functions revealed by Fourier transform scanning tunneling spectroscopy, *Phys. Rev. Lett.* 109 (2012) 116805.
- [15] F.D. Parmentier, T. Cazimajou, Y. Sekine, H. Hibino, H. Irie, D.C. Glattli, N. Kumada, P. Roulleau, Quantum Hall effect in epitaxial graphene with permanent magnets, *Sci. Rep.* 6 (2016) 38393.
- [16] K.S. Novoselov, Z. Jiang, Y. Zhang, S.V. Morozov, H.L. Stormer, U. Zeitler, J.C. Maan, G.S. Boebinger, P. Kim, A.K. Geim, Room-temperature quantum Hall effect in graphene, *Science* 315 (2007) 1379.
- [17] H. Cao, J. Tian, I. Miotkowski, T. Shen, J. Hu, S. Qiao, Y.P. Chen, Quantized Hall effect and Shubnikov–de Haas oscillations in highly doped Bi_2Se_3 : Evidence for layered transport of bulk carriers, *Phys. Rev. Lett.* 108 (2012) 216803.
- [18] S. Hill, S. Uji, M. Takashita, C. Terakura, T. Terashima, H. Aoki, J.S. Brooks, Z. Fisk, J. Sarrao, Bulk quantum Hall effect in $\eta\text{-Mo}_4\text{O}_{11}$, *Phys. Rev. B* 58 (1998) 10778–10783.

- [19] B.A. Bernevig, T.L. Hughes, S.-C. Zhang, Quantum spin Hall effect and topological phase transition in HgTe quantum wells, *Science* 314 (2006) 1757–1761.
- [20] M.Z. Hasan, C.L. Kane, Topological insulators, *Rev. Modern Phys.* 82 (2010) 3045–3067.
- [21] X.L. Qi, T.L. Hughes, S.C. Zhang, Topological field theory of time-reversal invariant insulators, *Phys. Rev. B* 78 (2008).
- [22] B.A. Bernevig, T.L. Hughes, *Topological Insulators and Topological Superconductors*, Princeton University Press, 2013.
- [23] S. Rachel, Interacting topological insulators: A review, *Rep. Progr. Phys.* 81 (2018) 116501.
- [24] T. Ozawa, H.M. Price, A. Amo, N. Goldman, M. Hafezi, L. Lu, M.C. Rechtsman, D. Schuster, J. Simon, O. Zilberberg, I. Carusotto, Topological photonics, *Rev. Modern Phys.* 91 (2019) 015006.
- [25] K. Ding, C. Fang, G. Ma, Non-Hermitian topology and exceptional-point geometries, *Nat. Rev. Phys.* 4 (2022) 745–760.
- [26] S. Ilani, J. Martin, E. Teitelbaum, J.H. Smet, D. Mahalu, V. Umansky, A. Yacoby, The microscopic nature of localization in the quantum Hall effect, *Nature* 427 (2004) 328–332.
- [27] R.A. Römer, J. Oswald, The microscopic picture of the integer quantum Hall regime, *Ann. Physics* 435 (2021) 168541.
- [28] J. Weis, K. von Klitzing, Metrology and microscopic picture of the integer quantum Hall effect, *Phil. Trans. R. Soc. A* 369 (2011) 3954–3974.
- [29] J. Oswald, Revision of the edge channel picture for the integer quantum Hall effect, *Results Phys.* 47 (2023) 106381.
- [30] D.B. Chklovskii, B.I. Shklovskii, L.I. Glazman, Electrostatics of edge channels, *Phys. Rev. B* 46 (1992) 4026–4034.
- [31] N.R. Cooper, J.T. Chalker, Coulomb interactions and the integer quantum Hall effect: Screening and transport, *Phys. Rev. B* 48 (1993) 4530–4544.
- [32] J. Oswald, R.A. Römer, Manifestation of many-body interactions in the integer quantum Hall effect regime, *Phys. Rev. B* 96 (2017a) 125128.
- [33] J. Oswald, R.A. Römer, Exchange-mediated dynamic screening in the integer quantum Hall effect regime, *Europhys. Lett.* 117 (2017b) 57009.
- [34] B.I. Halperin, J.K. Jain, Fractional quantum Hall effects, 2020.
- [35] B. Kramer, T. Ohtsuki, S. Kettemann, Random network models and quantum phase transitions in two dimensions, *Phys. Rep.* 417 (2005) 211–342.
- [36] K. Slevin, T. Ohtsuki, Critical exponent for the quantum Hall transition, *Phys. Rev. B* 80 (2009).
- [37] W. Li, C.L. Vicente, J.S. Xia, W. Pan, D.C. Tsui, L.N. Pfeiffer, K.W. West, Scaling in plateau-to-plateau transition: A direct connection of quantum Hall systems with the Anderson localization model, *Phys. Rev. Lett.* 102 (2009).
- [38] I.A. Gruzberg, A. Klümper, W. Nuding, A. Sedrakyan, Geometrically disordered network models, quenched quantum gravity, and critical behavior at quantum Hall plateau transitions, *Phys. Rev. B* 95 (2017) 125414.
- [39] M. Puschmann, P. Cain, M. Schreiber, T. Vojta, Integer quantum Hall transition on a tight-binding lattice, *Phys. Rev. B* 99 (2019) 121301.
- [40] A. Klümper, W. Nuding, A. Sedrakyan, Random network models with variable disorder of geometry, *Phys. Rev. B* 100 (2019) 140201.
- [41] R. Conti, H. Topchyian, R. Tateo, A. Sedrakyan, Geometry of random potentials: induction of two-dimensional gravity in quantum Hall plateau transitions, *Phys. Rev. B* 103 (2021).
- [42] D. Stauffer, A. Aharony, *Introduction to Percolation Theory*, second ed., Taylor & Francis Group, 1991.
- [43] P. Cain, R.A. Römer, Real-space renormalization-group approach to the integer quantum Hall effect, *Internat. J. Modern Phys. B* 19 (2005) 2085–2119.
- [44] Wolfram Research, Inc., *Mathematica V13.X*, Champaign, IL, 2022–2024.
- [45] J.T. Chalker, P.D. Coddington, Percolation, quantum tunnelling and the integer Hall effect, *J. Phys. C* 21 (1988) 2665–2679.
- [46] M.R. Zirnbauer, Marginal CFT perturbations at the integer quantum Hall transition, *Ann. Physics* 431 (2021) 168559.
- [47] A. Sedrakyan, Action formulation of the network model of plateau-plateau transitions in the quantum Hall effect, *Phys. Rev. B* 68 (2003) 235329.
- [48] J.T. Chalker, G.J. Daniell, Scaling, diffusion, and the integer quantized Hall effect, *Phys. Rev. Lett.* 61 (1988) 593–596.
- [49] B. Kramer, S. Kettemann, T. Ohtsuki, Localization in the quantum Hall regime, *Physica E* 20 (2003) 172–187.
- [50] F. Evers, W. Brenig, Semiclassical theory of the quantum Hall effect, *Phys. Rev. B* 57 (1998) 1805–1813.
- [51] P. Cain, R.A. Römer, M. Schreiber, M.E. Raikh, Integer quantum Hall transition in the presence of a long-range-correlated quenched disorder, *Phys. Rev. B* 64 (2001) 235326.
- [52] A.G. Galst'yan, M.E. Raikh, Localization and conductance fluctuations in the integer quantum Hall effect: Real-space renormalization-group approach, *Phys. Rev. B* 56 (1997).
- [53] D.-H. Lee, Z. Wang, S. Kivelson, Quantum percolation and plateau transitions in the quantum Hall effect, *Phys. Rev. Lett.* 70 (1993) 4130–4133.
- [54] L. Schweitzer, B. Kramer, A. MacKinnon, Magnetic field and electron states in two-dimensional disordered systems, *J. Phys. C* 17 (1984) 4111–4125.
- [55] B. Assi, A Study of the Integer Quantum Hall Effect with a Modified Chalker-Coddington Network Model that Incorporates Geometric Disorder (Ph.D. thesis), University of Warwick, 2019.
- [56] P. Cain, R.A. Römer, M.E. Raikh, R.A. Römer, Renormalization group approach to the energy level statistics at the integer quantum Hall transition, *Physica E* 18 (2003) 126–127.
- [57] P. Cain, M.E. Raikh, R.A. Römer, Real-space renormalization group approach to the quantum Hall transition, *J. Phys. Soc. Japan* 72 (2003) 135–136.
- [58] W.H. Press, S.A. Teukolsky, W.T. Vetterling, B.P. Flannery, *Numerical Recipes: The Art of Scientific Computing*, Cambridge University Press, 2007.
- [59] W. Nuding, A. Klümper, A. Sedrakyan, Localization length index and subleading corrections in a Chalker-Coddington model: A numerical study, *Phys. Rev. B* 91 (2015) 115107.
- [60] S. Koch, R.J. Haug, K. von Klitzing, K. Ploog, Experiments on scaling in $\text{Al}_x\text{Ga}_{1-x}\text{As}/\text{GaAs}$ heterostructures under quantum Hall conditions, *Phys. Rev. B* 43 (1991) 6828–6831.
- [61] K. Slevin, T. Ohtsuki, Corrections to scaling at the Anderson transition, *Phys. Rev. Lett.* 82 (1999) 382–385.
- [62] A. Rodriguez, L.J. Vazquez, K. Slevin, R.A. Römer, Critical parameters from a generalized multifractal analysis at the Anderson transition, *Phys. Rev. Lett.* 105 (2010) 046403.
- [63] A. Rodriguez, L.J. Vazquez, K. Slevin, R.A. Römer, Multifractal finite-size scaling and universality at the Anderson transition, *Phys. Rev. B* 84 (2011) 134209.
- [64] S. Shaw, R.A. Römer, Real-space renormalisation approach to the chalker-coddington model revisited: Improved statistics, in: WRAP: Warwick Research Archive Portal, University of Warwick, URL: <https://wrap.warwick.ac.uk/184136/>.
- [65] S. Shaw, R.A. Römer, DisQS/CCxD: Codes to simulate the real-space RG in variants of the Chalker-Coddington models, GitHub repository for the Disordered Quantum Systems Group, University of Warwick, URL: <https://github.com/DisQS/CCxD>.